ELSEVIER

# Melt mixing causes negative correlation of trace element enrichment and $CO_2$ content prior to an Icelandic eruption

CrossMark

David A. Neave [a,*], John Maclennan [a], Marie Edmonds [a], Thorvaldur Thordarson [b]

[a] Department of Earth Sciences, University of Cambridge, Downing Street, Cambridge CB2 3EQ, United Kingdom
[b] Faculty of Earth Sciences, University of Iceland, Askja, Sturlugata 7, 101 Reykjavik, Iceland

A B S T R A C T

Major elements, trace elements and volatiles were measured in 110 olivine-hosted melt inclusions from the subglacial Skuggafjöll eruption in the Eastern Volcanic Zone of Iceland. Variations in melt inclusion trace element concentrations can be accounted for by incomplete mixing of diverse mantle parental melts accompanied by variable extents of fractional crystallisation. Binary mixing between an incompatible trace element-enriched and depleted melts provides a good fit to observed variations in trace element ratios such as Ce/Y. Surprisingly, the $CO_2$ contents of melt inclusions correlate negatively with their degree of trace element enrichment. Depleted, low-Ce/Y inclusions with ∼1200 ppm $CO_2$ have high $CO_2/Nb$ contents (∼400), suggesting that melts experienced little or no $CO_2$ exsolution before inclusion entrapment. Enriched, high-Ce/Y inclusions contain ∼300 ppm $CO_2$, have low $CO_2/Nb$ (contents 50–100) and melts are likely to have exsolved much of their original $CO_2$ contents prior to inclusion entrapment. The negative correlation between $CO_2$ content and trace element enrichment may arise either from the more efficient exsolution of $CO_2$ from enriched melts, or from the intrusion of $CO_2$-supersaturated depleted melts into enriched melts that had already exsolved much of their original $CO_2$ contents. Some inclusions have lower $CO_2$ contents than predicted from binary mixing models, which suggests that at least some $CO_2$ exsolution occurred concurrently with mixing. Enriched inclusions record entrapment pressures of ∼0.5 kbar. These pressures probably correspond to the depth of mixing. Higher pressures recorded in depleted inclusions may have resulted from the development of $CO_2$ supersaturation during ascent from storage at ≥1.5 kbar. The presence of $CO_2$ supersaturation in melt inclusions has the potential to constrain timescales of melt inclusion entrapment.

## 1. Introduction

Dissolved volatile species play a crucial role in controlling the physical properties of silicate melts (e.g. Ochs and Lange, 1997; Giordano et al., 2008), determining the stability of crystal phases (e.g. Danyushevsky, 2001; Putirka, 2005) and driving eruptions (e.g. Blake, 1984; Woods, 1995; Roggensack et al., 1997). Furthermore, volatiles play an important role in mantle melting (e.g. Green, 1973; Eggler, 1976; Wyllie and Huang, 1976). Direct determination of the concentration and distribution of volatiles in primary melts and hence the mantle is difficult because volatiles often exsolve from melts prior to eruption. The solubility of $CO_2$ in basaltic melts is significantly less than that of $H_2O$, S, F or Cl, and depending on their initial $CO_2$ concentration, melts may become saturated with a $CO_2$-dominated vapour at depths of 25 km or more (Dixon, 1997; Shishkina et al., 2010; Ni and Keppler, 2013). Melt inclusions trapped in primitive crystals during early phases of magmatic evolution can provide estimates of initial volatile contents, but are prone to post-entrapment modification (e.g. Danyushevsky et al., 2000; Steele-Macinnis et al., 2011) and, in the case of $H_2O$, re-equilibration with their host melt (e.g. Qin et al., 1992; Hauri, 2002; Portnyagin et al., 2008; Gaetani et al., 2012).

Rare examples of glasses quenched from undersaturated melts have been reported in the literature: Saal et al. (2002) describe a positive correlation between $CO_2$ and Nb in matrix glasses and melt inclusions from the Siqueiros fracture zone on the East Pacific Rise that is indicative of vapour undersaturation, where both $CO_2$ and Nb behave incompatibly during fractionation. $CO_2$ fluxes have been calculated from Nb concentrations in a number of magmatic settings using $CO_2/Nb$ values assumed to be representative of undegassed primary melts (e.g. Workman et al., 2006; Cartigny et al., 2008; Shaw et al., 2010). However, estimates of
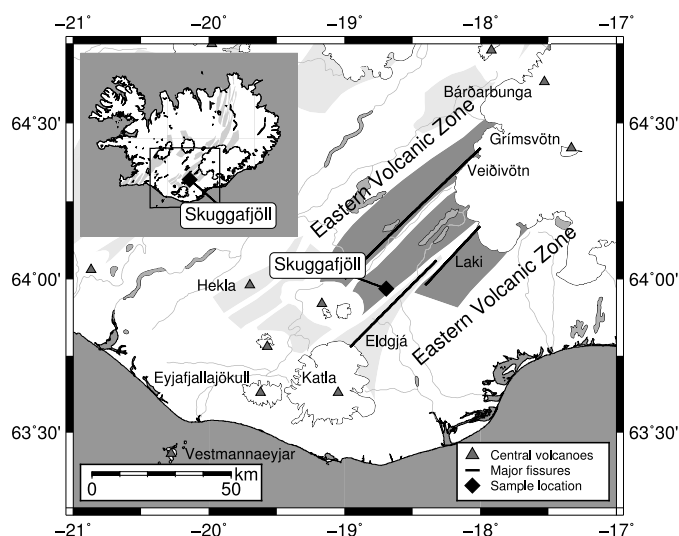
**Fig. 1.** Map showing the location of Skuggafjöll within the Eastern Volcanic Zone (EVZ) of Iceland. Central volcanoes and major fissure eruptions are labelled. Fissure swarms in the northeastern region of the EVZ associated with tholeiitic volcanism are shown as dark shaded regions (Thordarson and Larsen, 2007, and references therein). Fissure swarms associated with alkalic or transitional volcanism are shown as pale shaded regions.

primary $CO_2/Nb$ vary depending on location and measurement method: the value of $239 \pm 46$ for Siqueiros determined from direct analysis of glass by Saal et al. (2002) lies at the lower end of the global range, whereas values of ∼570 and ∼730 for 14°N and 34°N on the Mid-Atlantic Ridge reconstructed from lava $\delta^{13}C$ contents by Cartigny et al. (2008) lie towards the upper end. The only estimate of undegassed $CO_2/Nb$ from an Icelandic magma is $314 \pm 125$ from the Borgarhraun lava flow (Hauri et al., 2002).

Calculations using $CO_2/Nb$ to determine initial $CO_2$ contents generally assume that magmas evolve along a single liquid line of descent from a primary melt with a specific Nb content. However, it is well known from melt inclusion studies of single eruptions in Iceland that primary melts are highly heterogeneous in terms of their trace element and isotope compositions (e.g. Gurenko and Chaussidon, 1995; Slater et al., 2001; Maclennan et al., 2003; Maclennan, 2008b). Whether primary melt heterogeneity results from the melting process or from mantle source variability, it is expected that undegassed, enriched melts with high Nb contents would also have high $CO_2$ contents (Cartigny et al., 2008). In this case, a positive correlation between $CO_2$, Nb and the degree of melt enrichment recorded by trace element ratios such Ce/Y would be predicted. In order to use $CO_2/Nb$ to quantify magmatic carbon budgets, a good understanding of what controls $CO_2/Nb$ during magmatic evolution and melt mixing is required. Iceland is an ideal location to investigate the behaviour of $CO_2$ in primitive melts, because magma may be stored at depths where vapour saturation is unlikely (e.g. Winpenny and Maclennan, 2011).

We present major element, trace element and volatile data from 110 olivine-hosted melt inclusions from the primitive Skuggafjöll eruption in the Eastern Volcanic Zone (EVZ) of Iceland (Fig. 1). By considering trace element data alongside volatile data, we demonstrate that the $CO_2$ content of melt inclusions is controlled by mixing between geochemically distinct parental melts that have experienced different extents of $CO_2$ exsolution prior to melt inclusion entrapment. Our results also highlight the risks of interpreting melt inclusion volatile data without the corresponding trace element data. In the absence of trace element data, the volatile systematics we have observed might have been interpreted erro-

neously using models involving open-system degassing, conduit convection or gas flushing processes.

## 2. Sample collection and analytical methods

Skuggafjöll is an ∼820 m high mountain in the EVZ between the Vatnajökull and Mýrdalsjökull glaciers (Fig. 1; 63.968°N, 18.695°W). The mountain forms part of a northeast–southwest-striking hyaloclastite ridge (or tindar), and is likely to have formed during the last glacial period (Jakobsson and Gudmundsson, 2008). The lower flanks of the mountain are composed of vesicular, highly phyric, glassy pillow basalts, whereas the upper portions are composed of hyaloclastite, containing up to fist-sized lithics of pillow basalt and individual macrocrysts in a palagonite matrix.

Olivine macrocrysts in the size range 0.25 mm to 3 mm were picked from crushed pillow glasses collected from three localities at the base of the mountain. Care was taken to select pale green, unaltered olivine macrocrysts that contained glassy melt inclusions without post-entrapment daughter crystals. Macrocrysts were individually mounted in CrystalBond™ and polished to expose melt inclusions before being re-mounted in Buehler EpoThin™ resin and re-polished for analysis.

Melt inclusions were analysed for trace elements, $H_2O$, F and $CO_2$ by secondary ion mass spectrometry (SIMS). Major elements and S were determined by electron probe microanalysis (EPMA). SIMS analyses were performed using a Cameca ims-4f instrument at the NERC Ion Microprobe Facility at the University of Edinburgh, UK. $CO_2$ analyses were performed first, with a high mass resolution configuration, in order to enable good separation of $^{12}C$ and $^{24}Mg^{2+}$ peaks. $H_2O$, F and trace elements were then measured with a lower mass resolution configuration. $CO_2$, $H_2O$, F and trace elements of low abundance, such as Yb and Lu, were measured with a $1\sigma$ precision of $\pm10\%$. Trace elements of high abundance, such as Zr and Sr, were measured with a $1\sigma$ precision of $\pm5\%$. Errors in $CO_2$ and $H_2O$ were determined using repeat analyses of a suite of basaltic glass standards with compositions given by Shishkina et al. (2010). Errors in F and trace elements were determined using repeat analyses of international standards, ML3B-G, BCR-2G and GOR132-G. EPMA analyses were performed using a Cameca SX100 instrument at the Department of Earth Sciences at the University of Cambridge, UK. Full details of analytical procedures, as well as SIMS and EPMA data, are provided in the supplementary material.

Raman spectroscopy (e.g. Frezzotti et al., 2012) and heating/cooling stage experiments (e.g. Hansteen and Klugel, 2008) were undertaken prior to SIMS analyses in order to determine the $CO_2$ content of inclusion-hosted bubbles. If $CO_2$ is present in inclusion-hosted bubbles, it must be accounted for when calculating the total $CO_2$ content of melt inclusions (e.g. Hartley et al., 2014). More than 200 olivine grains containing bubble-bearing inclusions were mounted in CrystalBond™ for analysis by Raman spectroscopy using a Horiba LabRam™ instrument at the University of Cambridge, UK. The detection limit of $CO_2$ in inclusion-hosted bubbles is better than 0.04 g/cm$^3$ based analysis of $CO_2$-bearing samples on the same instrument (Hartley et al., 2014). Ten olivine grains containing bubble-bearing inclusions were individually polished and investigated using a Linkham THMS650 heating/cooling stage interfaced with a Zeiss Axioscope™ microscope. Olivine grains were cooled to $-90$°C before being heated slowly to 35°C, in order to observe of phase change temperatures within bubbles (Hansteen and Klugel, 2008). The detection limit of $CO_2$ is similar to that estimated for Raman spectroscopy by Hartley et al. (2014) (e.g. Rosso and Bodnar, 1995).
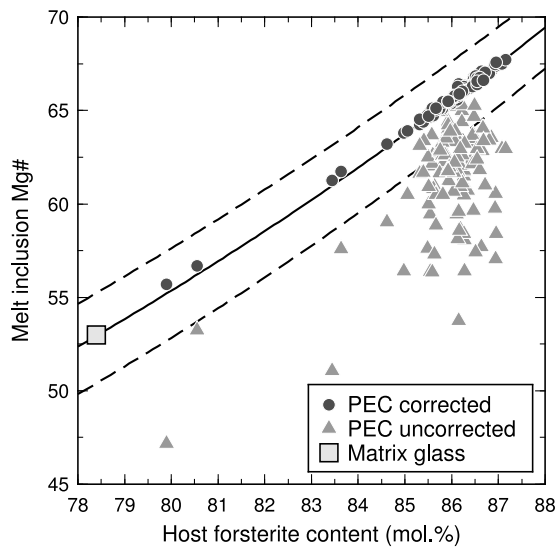
**Fig. 2.** Plot of host olivine forsterite content versus melt inclusion Mg#. Melt inclusion compositions are plotted before (triangles) and after (circles) post-entrapment crystallisation (PEC) correction. PEC corrections were performed using PETROLOG3 (Danyushevsky and Plechov, 2011). The olivine forsterite content in equilibrium with the matrix glass is shown as a large square. Constant $K_d^{ol-liq}_{Fe-Mg}$ values of 0.31 are shown by the black solid line, with errors of $\pm 0.03$ shown as dashed lines.

## 3. Results

### 3.1. Major elements

Olivine macrocrysts from Skuggafjöll have compositions in the range $Fo_{79}$ to $Fo_{87}$. 106 of the 110 melt inclusions analysed were hosted in high-forsterite macrocrysts with core compositions in the range $Fo_{84}$ to $Fo_{87}$ (Fig. 2). $Fo_{87}$ olivines from Skuggafjöll are slightly more primitive than the most primitive olivines from Laki to the southeast ($Fo_{86}$; Neave et al., 2013), and are amongst the most primitive olivines from the EVZ (c.f. Hansen and Grönvold, 2000; Passmore, 2009; Moune et al., 2012). Matrix glasses from Skuggafjöll are tholeiitic in composition, indicating that the eruption is probably affiliated with the Bárdarbunga–Veidivötn volcanic system (Jakobsson, 1979).

Melt inclusion compositions range from Mg# $\sim$55 to Mg# $\sim$67.5 (Fig. 2). The major element composition of melt inclusions can be affected by post-entrapment crystallisation (PEC), where continued crystallisation of olivine on melt inclusion walls after entrapment leads to a drop in melt inclusion Mg# (e.g. Danyushevsky et al., 2000, 2002). This drop is visible in Fig. 2, where the Mg# of melt inclusions is lower than that predicted from the forsterite content of the host olivine using $K_d^{ol-liq}_{Fe-Mg} \sim 0.31$. Although olivine macrocrysts can undergo diffusive re-equilibration with their surroundings after formation (e.g. Costa and Morgan, 2010; Thomson and Maclennan, 2013), using olivine forsterite content as a proxy for the degree of melt inclusion evolution instead of melt inclusion Mg# avoids complications arising from PEC. The extent of PEC was estimated using PETROLOG3 (Danyushevsky and Plechov, 2011). Calculations suggest that while some inclusions have experienced up to 5% PEC, most have only experienced $\sim$2%. PEC corrections are therefore minor.

### 3.2. Trace elements

Signal-to-noise ratios ($\sigma_t/\sigma_r$, where $\sigma_t$ is the true variation in a sample set and $\sigma_r$ an estimate of analytical error) were calculated for all elements analysed in order to assess the contributions of natural variation and analytical error to the generation sample
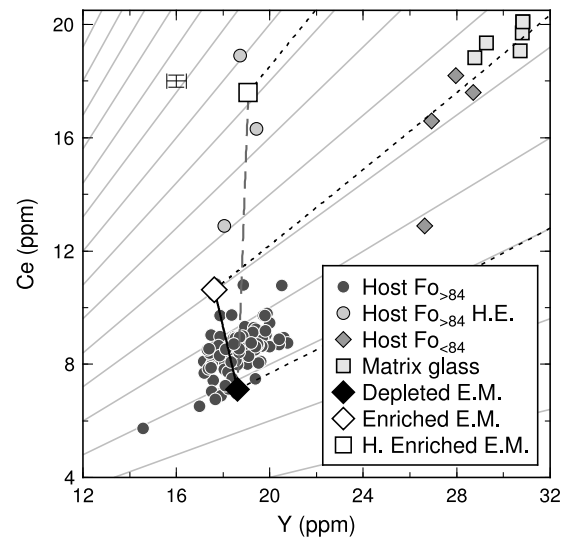


**Fig. 3.** Plot summarising trace element variability in melt inclusions and matrix glasses from Skuggafjöll. Melt inclusions are divided into the following populations: primitive (host $Fo_{>84}$), shown as dark grey circles; highly-enriched (H.E.) and primitive (host $Fo_{>84}$ and Ce/Y > 0.65), shown as pale grey circles; and evolved (host $Fo_{<84}$), shown as mid grey diamonds. A mixing line between depleted and enriched end-members (E.M.s) is shown as a solid black line. A mixing line between depleted and highly enriched end-members is shown as a dashed grey line. Depleted, enriched and highly-enriched end-members are shown as a black diamond, a white diamond and a white square respectively. Lines of constant ratio are shown as solid pale grey lines. Fractional crystallisation paths for each of the end-members are shown as dark dotted lines. $2\sigma$ error bars are shown.

variability. $\sigma_t$ was determined following the method of Maclennan et al. (2003) by using the relationship $\sigma_t^2 = \sigma_o^2 - \sigma_r^2$, where $\sigma_o$ is the observed variation. The $\chi^2$ distribution was used to assess the quality of $\sigma_r$, which depends on the number of repeat analyses used to estimate analytical precision, in order to test whether signal-to-noise ratios are significant at a given confidence level. Signal-to-noise ratios for both element concentrations and element ratios are provided in the supplementary material. Signal-to-noise ratios for most trace elements are greater than the threshold for significant variability at the 95% confidence interval. Signal-to-noise ratios are high for incompatible and abundant elements. For example, Ce has a higher signal-to-noise ratio ($\sigma_t/\sigma_r = 14.6$) than both Nb ($\sigma_t/\sigma_r = 5.3$), which is more incompatible but less abundant, and Y ($\sigma_t/\sigma_r = 4.4$), which is less incompatible and similarly abundant. Some elements that were analysed with low precision have low signal-to-noise ratios, such as Sm ($\sigma_t/\sigma_r = 1.7$), and it is not possible to resolve natural variability through analytical noise. Y was measured with higher precision than Yb and consequently Ce/Y has a higher signal-to-noise ratio than Ce/Yb ($\sigma_t/\sigma_r = 7.5$ and 3.0 respectively).

Two main populations of melt inclusions are defined on the basis of their trace element and host olivine composition (Figs. 3 and 4). Melt inclusions hosted in $Fo_{<84}$ macrocrysts have high concentrations of moderately incompatible elements (Y > 26 ppm) and possess trace element ratios most similar to the matrix glass (Ce/Y $\sim$ 0.63 in $Fo_{<84}$ inclusions and $\sim$0.65 in matrix glasses). $Fo_{<84}$ inclusions are henceforth referred to as evolved melt inclusions. Melt inclusions hosted in $Fo_{>84}$ macrocrysts are characterised by low concentrations of moderately incompatible elements (Y < 22 ppm) and are referred to as primitive melt inclusions. A sub-population of three highly enriched primitive melt inclusions is also defined on the basis of having Ce/Y > 0.65. Trace element concentrations in primitive melt inclusions vary by up to a factor of $\sim$3.5 (Fig. 3), and Ce/Y ranges from 0.37 to 1.01. These values lie well within the range known from elsewhere in Iceland (e.g.
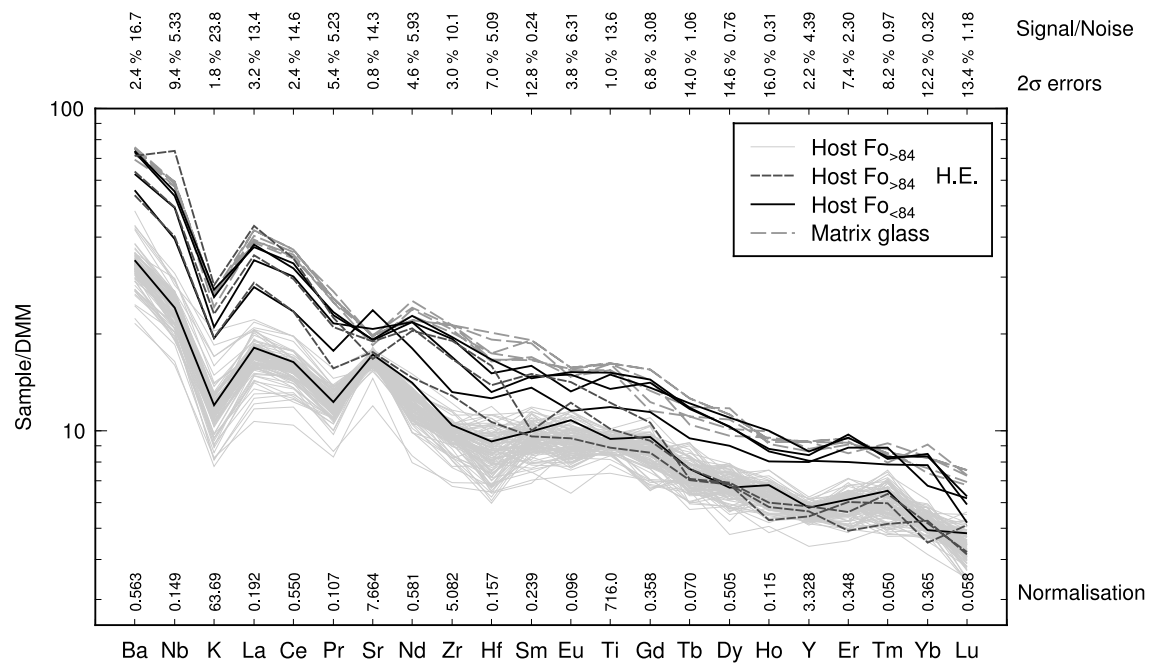
**Fig. 4.** Depleted MORB mantle (DMM; Workman and Hart, 2005) normalised multi-element diagram for melt inclusions and matrix glasses from Skuggafjöll. Highly-enriched (H.E.) and evolved melt inclusions are distinguished from the primitive inclusions. $2\sigma$ errors are shown along the top of the plot and DMM normalisation values along the bottom. The degree of variability in primitive melt inclusions is expressed as a signal-to-noise ratio for each element measured. Signal-to-noise ratios in excess of 2.83 indicate that variability is significant at the 99% confidence level.

Slater et al., 2001; Gurenko and Sobolev, 2006; Maclennan, 2008a; Neave et al., 2013).

### 3.3. Volatiles

Different volatile species show remarkably different amounts of variability in melt inclusions from Skuggafjöll. $H_2O$–$CO_2$ systematics are summarised in Fig. 5a. $CO_2$ concentrations vary by a factor of $\sim$7 in primitive melt inclusions, with $CO_2$ concentrations ranging from 175 ppm to 1202 ppm. Evolved melt inclusions generally have $\sim$450 ppm $CO_2$, with the exception of one inclusion that contains 782 ppm. $CO_2$ concentrations in matrix glasses are below the detection limit (<25 ppm). $H_2O$ exhibits very limited variability, with $H_2O$ contents of $0.39 \pm 0.05(1\sigma)$ wt% and $0.36 \pm 0.03(1\sigma)$ wt% found in melt inclusions and matrix glasses respectively.

F measured in melt inclusions by SIMS does not show significant variability, which may indicate open system behaviour (e.g. Koleszar et al., 2009). Primitive melt inclusions have a mean F content of $213 \pm 35(1\sigma)$ ppm, evolved melt inclusions a mean F of $309 \pm 85(1\sigma)$ ppm and matrix glasses a mean F of $404 \pm 31(1\sigma)$ ppm. Cl concentrations were below the detection limit of EPMA (200 ppm from counting statistics), and thus were not reliably measurable. S measured by EPMA does not show significant variability. Melt inclusions have a mean S content of $607 \pm 94(1\sigma)$ ppm, evolved melt inclusions a mean S of $725 \pm 93(1\sigma)$ ppm and matrix glasses a mean S of $622 \pm 83(1\sigma)$ ppm.

### 3.4. Inclusion-hosted bubbles

Where present, inclusion-hosted bubbles make up $\sim 1.6 \pm 0.6(1\sigma)\%$ of melt inclusion volumes. No Fermi doublets were observed in any of the $\sim$200 bubbles analysed for $CO_2$ by Raman spectroscopy. No changes in appearance were observed in the inclusion-hosted bubbles investigated during heating/cooling stage

experiments. We therefore conclude that bubbles contain either no $CO_2$, or $CO_2$ at concentrations below the detection limit of $\sim$0.04 g/cm$^3$.

### 3.5. Element correlations

Cross-correlation matrices for key major element, trace element and volatile species in primitive melt inclusions from Skuggafjöll are shown in Fig. 6. Separate matrices are provided for datasets that include and exclude highly enriched inclusions. Elements analysed with low precision (e.g. F and Sm), or that are strongly affected by PEC or diffusive alteration (e.g. MgO, FeO and $H_2O$), are excluded to prevent the identification of correlations not related to primary magmatic processes. Elements that are highly incompatible during mantle melting, (e.g. Ba, Nb, Ce, Zr), correlate very strongly with each other ($r > 0.9$). Incompatible elements measured by SIMS also correlate ($r > 0.6$) with incompatible elements measured by EPMA (e.g. $TiO_2$, $K_2O$, $P_2O_5$). However, highly incompatible elements do not correlate with elements that are more compatible during mantle melting (e.g. Y, Yb). Principal component analysis (e.g. Albarède, 1996; McKenzie and O'Nions, 1998) confirms that most variability in trace element concentrations is correlated: 84% of the variance within the dataset is explained by the first principal component.

Perhaps the most striking feature of the covariance structure in Fig. 6 is that $CO_2$ correlates negatively with incompatible elements such as Nb ($r = -0.35$). If the three highly enriched inclusions, which could be sourced from a different macrocryst population from that hosting most of the primitive inclusions, are excluded, $CO_2$–trace element correlations, including that between $CO_2$ and Nb ($r = -0.56$), are stronger. This negative correlation between $CO_2$ and Nb (Fig. 7a) contrasts with the positive correlations measured in undegassed melt inclusions from the Siqueiros fracture zone on the East Pacific Rise (Saal et al., 2002) and calculated for undegassed Mid-Atlantic Ridge basalts (Cartigny et al., 2008). Other $CO_2$–trace element datasets either record significant variability in
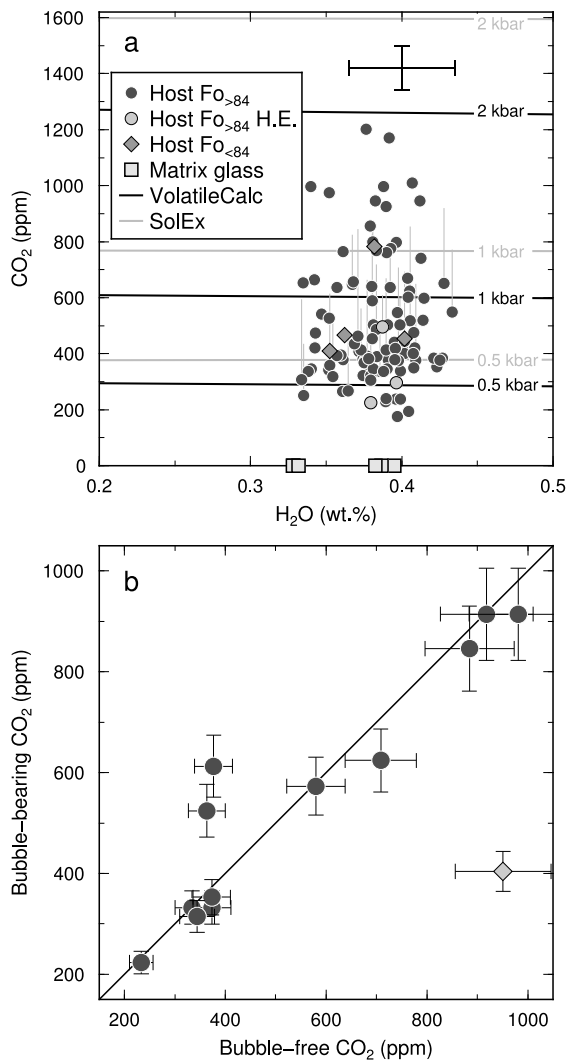
**Fig. 5.** (a) $H_2O$ and $CO_2$ contents of melt inclusions and matrix glasses overlaid onto isobars calculated using VOLATILECALC (Newman and Lowenstern, 2002) and SOLEX (Witham et al., 2012) that are shown as dark and pale solid line respectively. Vertical pale grey lines show maximum possible $CO_2$ contents of bubble-bearing melt inclusions assuming that $CO_2$ is present in inclusion-hosted bubbles at densities equivalent to the Raman detection limit. $2\sigma$ error bars are shown. (b) $CO_2$ contents of bubble-free and bubble-bearing melt inclusions within individual olivine grains. Most points lie close to the 1:1 line shown as a solid black line. Melt inclusions from one macrocryst that are plotted as a diamond lie well from the 1:1 line, but these inclusions have significantly different trace element contents: the $CO_2$-poor bubble-bearing inclusion has Ce/Y $\sim 0.46$, whereas the $CO_2$-rich bubble-free inclusion has Ce/Y $\sim 0.39$.

$CO_2$ with near-constant Nb (Shaw et al., 2010), or show no robust correlations between the two species (Dixon and Clague, 2001; Dixon et al., 2008; Workman et al., 2006; Koleszar et al., 2009; Helo et al., 2011).

## 4. Discussion

### 4.1. Inclusion-hosted bubbles and total $CO_2$ contents of melt inclusions

Both volume changes and diffusive loss of volatiles can lead to the nucleation of bubbles within melt inclusions during cooling (Roedder, 1979, 1984; Lowenstern, 1995; Steele-Macinnis et al., 2011). Associated drops in melt inclusion pressures may lead to the sequestration of $CO_2$ into these bubbles (Bucholz et al., 2013; Hartley et al., 2014). For example, Anderson and Brown (1993) suggest that a significant quantity of $CO_2$ was transferred from melt

to bubbles in bubble-bearing inclusions from Kīlauea Iki, Hawai'i, prior to quenching, leading to the underestimation of melt inclusion entrapment pressures by up to 1 kbar. However, the inability to detect $CO_2$ in inclusion-hosted bubbles by either Raman spectroscopy or heating/cooling stage experiments in samples from Skuggafjöll suggests that $CO_2$ is either absent or present at concentrations below the detection limit. Maximum $CO_2$ contents for bubble-bearing inclusions can be estimated from inclusion and bubbles sizes, assuming that $CO_2$ is present at a density equivalent to the detection limit of 0.04 g/cm$^3$. In this case, an extra $225 \pm 85(1\sigma)$ ppm of $CO_2$ would be added to bubble-bearing inclusions. Calculated maximum $CO_2$ contents of bubble-bearing inclusions are shown as grey error bars in Figs. 5 and 7. Full calculation results, as well as bubble and inclusion dimensions, are provided in the supplementary material.

During SIMS analysis, it was possible to analyse paired melt inclusions within 11 olivine grains where one inclusion possessed a bubble and the other did not. In the majority of cases the two melt inclusions have the same $CO_2$ concentration within error (Fig. 5b). In just one case the bubble-bearing inclusion has significantly less $CO_2$ than the bubble-free inclusion (shown as a diamond in Fig. 5b). However, these two inclusions possess different trace element contents, suggesting that they trapped geochemically distinct melts, rather than that the bubble-bearing inclusion has sequestered $CO_2$ into a bubble.

Although $CO_2$ was not detected in any of the inclusion-hosted bubbles analysed in this study, we consider here the possibility that bubbles lost $CO_2$ after entrapment. To this end, we calculate the theoretical amount of $CO_2$ in bubbles if they were in equilibrium with their host melt inclusion at the time of quenching using the method of Shaw et al. (2008, 2010). The mass of $CO_2$ in bubbles was calculated using the ideal gas law ($n = PV/RT$), where bubble pressures were determined from the concentration of $CO_2$ in melt inclusion glasses (Witham et al., 2012) and temperature was taken as the glass transition temperature (700 °C; Shaw et al., 2008). Total $CO_2$ contents of corrected bubble-bearing melt inclusions lie in the range 1431–5145 ppm (Supplementary Fig. B1), which is well in excess of the range of $CO_2$ contents measured in bubble-free inclusions (173–1202 ppm). Calculated equilibrium bubble $CO_2$ densities lie in the range 0.26–0.82 g/cm$^3$, and are thus well above the detection limits of both Raman spectroscopy and heating/cooling stage experiments. Calculation results are provided in the supplementary material. Given the disparity between corrected bubble-bearing and bubble-free inclusions and the extent of $CO_2$ leakage required to equalise $CO_2$ contents between corrected and uncorrected inclusions, we conclude that it is unlikely that the melt and bubble portions of melt inclusions attained $CO_2$ equilibrium before quenching. $CO_2$ concentrations measured in the glassy portions of melt inclusions are therefore likely to represent the total inclusion $CO_2$ contents.

Although inclusion-hosted bubbles do not contain significant quantities of $CO_2$, it is nevertheless important to consider how melt-bubble disequilibrium may occur within melt inclusions. Bubbles that result from the difference in thermal expansion between melt inclusions and their host crystals may be vacuums if melt inclusions are volatile-free (Steele-Macinnis et al., 2011). If melt inclusions are quenched rapidly upon eruption, as is the case for the subglacial Skuggafjöll, we suggest that $CO_2$ may be unable to diffuse through silicate portions of inclusions and into bubbles. Bubble-melt $CO_2$ equilibrium at Skuggafjöll may have been kinetically limited by rapid quenching and the comparatively slow diffusion of $CO_2$ in silicate liquids (e.g. Ni and Keppler, 2013). We propose that the inclusion-hosted bubbles investigated here are close to being vacuums, and contain, at most, trace quantities of $CO_2$ and insoluble noble gases. A detailed treatment of the post-entrapment behaviour of $CO_2$ in olivine-hosted melt inclu-
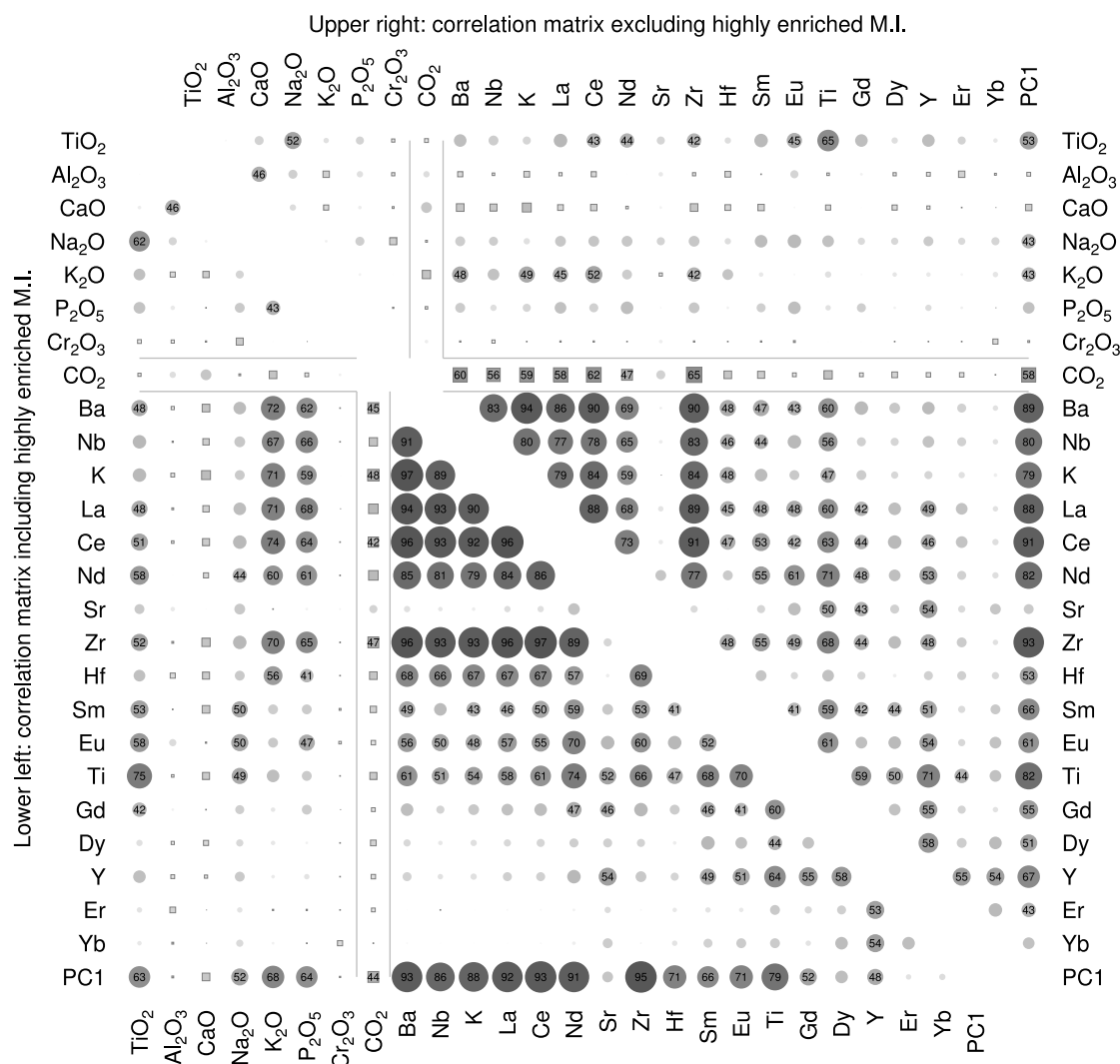
**Fig. 6.** Cross-correlation matrices of selected elements and the first principal component (PC1) in primitive Skuggafjöll melt inclusions including and excluding highly-enriched inclusions. The triangular matrix in the lower left half of the figure shows correlations including highly-enriched inclusions show whereas the triangular matrix in the upper right half shows correlations excluding highly-enriched inclusions. Large dark symbols show strong correlations and small pale symbols, weak correlations. $r$ values multiplied by 100 are shown in the centre of symbols for correlations better than $r = \pm 0.4$. Positive correlations (e.g. between Ba and Nb) are shown by circles with shaded fill. Negative correlations (e.g. between $CO_2$ and Nb) are shown by squares with shaded fill. Pale lines separate oxides measured by EPMA from $CO_2$ and trace elements measured by SIMS. Note the strong correlations between highly incompatible elements and the negative correlation of $CO_2$ with highly incompatible trace elements. The negative correlation between $CO_2$ and incompatible trace elements is stronger when highly-enriched inclusions are excluded.

sions could provide insights into cooling timescales, but is beyond the scope of this work. It is important to note, however, that the following discussions do not depend on observations from bubble-bearing inclusions: discarding bubble-bearing inclusions does not significantly affect the $CO_2$-trace element systematics we observe.

### 4.2. $H_2O$, diffusive re-equilibration and subglacial eruption

Open system behaviour of $H_2O$, where melt inclusions have much lower $H_2O$ contents than would be expected at magma reservoir pressures, has been reported in a number of natural melt inclusion suites (e.g. Hauri, 2002; Koleszar et al., 2009). Recent experimental studies have confirmed that the $H_2O$ contents of olivine-hosted melt inclusions can re-equilibrate with their host melt within hours at magmatic temperatures of $\sim$1200 °C by $fO_2$-independent $H^+$ diffusion (Gaetani et al., 2012; Bucholz et al., 2013). The near-uniform $H_2O$ contents of melt inclusions and matrix glasses from Skuggafjöll (Fig. 5a) suggest that the melt inclusions re-equilibrated with their carrier liquid shortly before eruption.

Equilibration pressures of $\sim$1.4 MPa and $\sim$5.3 MPa are calculated for Skuggafjöll matrix glasses with an $H_2O$ content of 0.36 wt% and $CO_2$ contents of 0 ppm and 25 ppm respectively (Witham et al., 2012). The $CO_2$ concentration of 25 ppm corresponds to the detection limit by SIMS. Elevated pressures recorded in matrix glass compositions are consistent with eruption beneath a glacier (e.g. Höskuldsson et al., 2006). 1.4–5.3 MPa corresponds to a range in ice/water thickness of 140–530 m, assuming a density of 1 Mg/m$^3$ for the overlying material. An ice thickness of $\leq$530 m is substantially less than the $\sim$1500 m estimated for central Iceland at the last glacial maximum by Hubbard et al. (2006), which may indicate that eruption took place in evacuated melt water pools or at a time of reduced ice thickness (e.g. Tuffen et al., 2010; Owen et al., 2012).

### 4.3. Trace element variability and binary mixing

Binary mixing models between depleted and enriched end-members are often successful in explaining incompatible trace element and isotope variability in primitive basalts (e.g. Zindler
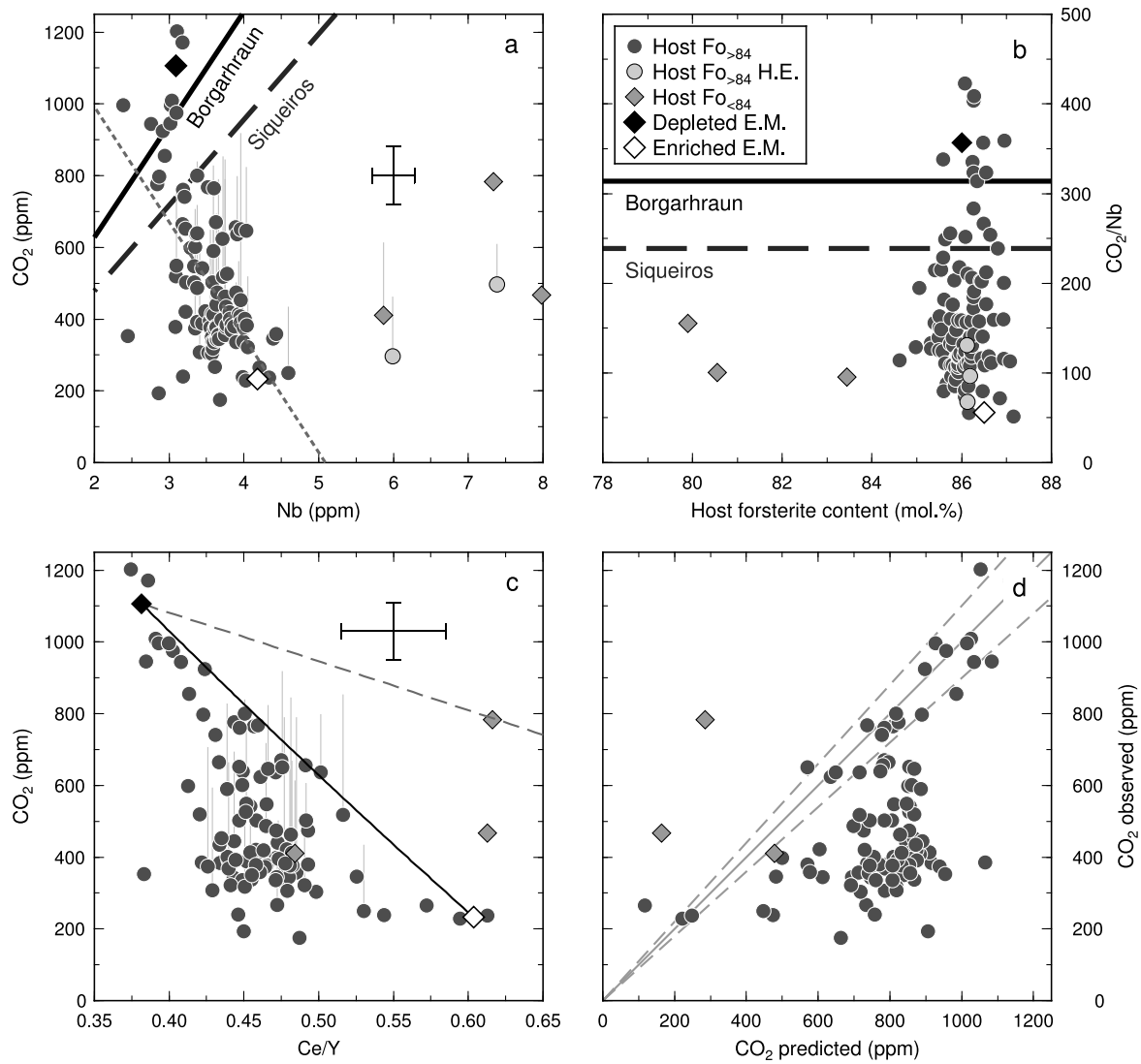
**Fig. 7.** (a) Plot of $CO_2$ versus Nb. Average $CO_2$/Nb values for Siqueiros (Saal et al., 2002) and Borgarhraun (Hauri et al., 2002) are shown as dashed and solid dark lines respectively. A negative correlation is observed between Nb and $CO_2$ for primitive melt inclusion data. This negative correlation is illustrated by the least squares regression through $Fo_{>84}$-hosted inclusions shown by the dark dotted line. Vertical pale grey lines show the maximum possible $CO_2$ contents of bubble-bearing melt inclusions. $2\sigma$ error bars are shown. (b) Plot of melt inclusion $CO_2$/Nb versus host forsterite content. Primitive melt inclusions exhibit a large range of $CO_2$/Nb contents that exceed mean values from both Siqueiros and Borgarhraun. (c) Plot of $CO_2$ versus Ce/Y with the Ce/Y axis expanded to show variability within the primitive melt inclusion population. A mixing line between depleted and enriched end-members is shown as a solid black line. A mixing line between depleted and highly-enriched end-members is shown as a dashed grey line. Note that while many inclusions lie along the mixing line between depleted and enriched end-members, many lie to lower $CO_2$ contents. Vertical pale grey lines show the maximum possible $CO_2$ contents of bubble-bearing melt inclusions. $2\sigma$ error bars are shown. (d) Plot of $CO_2$ observed in melt inclusions versus the $CO_2$ content predicted using binary mixing calculations between depleted and enriched end-members. A one-to-one line is shown as a solid line, with dashed lines showing $2\sigma$ errors in $CO_2$ analyses.

et al., 1984; Maclennan, 2008b; Waters et al., 2011). In the case of Skuggafjöll, two mixing scenarios were considered: firstly, between depleted and enriched end-members and secondly, between depleted and highly enriched end-members (Fig. 3). A depleted end-member was calculated as the average of the three lowest Ce/Y primitive inclusions and an enriched end-member as the average of the two highest Ce/Y primitive inclusions, excluding the three highly enriched primitive inclusions. A highly enriched end-member was defined as the average of the two highest Ce/Y inclusions in the whole dataset.

The ability of binary mixing and fractional crystallisation to account for the diversity of melt inclusion compositions was assessed quantitatively using the method of Maclennan (2008a). The following forward model was set up in order to determine the best fitting fraction of enriched end-member ($X_e$) and extent of fractional crystallisation ($F$) for each melt inclusion given specified

enriched and depleted end-member compositions ($C_e$ and $C_d$):

$$C = \left[ X_e C_e + (1 - X_e) C_d \right] (1 - F)^{D-1} \tag{1}$$

where $C$ is the concentration of an element in a melt inclusion and $D$ is the bulk partition coefficient of the assemblage removed during fractional crystallisation. Bulk $D$ values assume crystallisation of a gabbroic assemblage at 1200 °C and 0.5 kbar. Partition coefficients were calculated using the models of Bindeman and Davis (2000) and Blundy and Wood (1991) for plagioclase, Wood and Blundy (1997) and Hill et al. (2010) for clinopyroxene and Bédard (2005) for olivine. The misfit function between predicted and observed compositions was defined as:

$$\Theta = \sum_{i=1}^{N} \left( \frac{C_i^{obs} - C_i^{calc}}{\sigma_i} \right)^2 \tag{2}$$

where the difference between observed and calculated compositions ($C_i^{obs} - C_i^{calc}$) was divided by the precision ($\sigma_i$) in order to weight the misfit function in favour of well-measured elements.

The mean misfit between the observed and predicted melt inclusion compositions is less than 5% for all fitted elements (except Lu; ~7%) when considering mixing between depleted and enriched end-members. The standard deviation of the misfit is similar to the analytical uncertainty (<15% for all cases), and is less than 5% for well measured elements such as Ti, Sr, Ce, Y. The values of $X_e$ returned from the fits correlate extremely well with observed Ce/Y values ($r = 0.96$). Trace element variability in most melt inclusions from Skuggafjöll can therefore be explained well by a combination of magma mixing and fractional crystallisation. Although the compositions of highly enriched melt inclusions can be accounted for by mixing between depleted and highly-enriched end-members, how the three highly-enriched inclusions relate to other primitive inclusions is unclear. Nevertheless, all three mixing end-members are within the compositional range known from other Icelandic systems, and are therefore feasible parental melt compositions (e.g. Slater et al., 2001; Gurenko and Sobolev, 2006; Maclennan, 2008a; Neave et al., 2013). The end-members are likely to have formed by mixing of more diverse primitive melts during deeper storage (e.g. Maclennan, 2008a) or transport from the melt source region (e.g. Rudge et al., 2013).

### 4.4. Generating a negative correlation between trace element enrichment and CO₂ content

If CO₂ and Nb both behaved incompatibly during the evolution and mixing of the Skuggafjöll magma, they would correlate positively (e.g. Saal et al., 2002). While poor correlations between CO₂ and incompatible trace elements can be explained by variable extents of CO₂ exsolution prior to melt inclusion entrapment (e.g. Koleszar et al., 2009), negative correlations such as those observed at Skuggafjöll appear unlikely to have arisen from haphazard exsolution of CO₂ alone. Generating a negative correlation between CO₂ and Nb by concurrent CO₂ exsolution and fractional crystallisation can be ruled out because CO₂ also correlates negatively with trace element ratios that can only be fractionated significantly during mantle melting, such as Ce/Y ($r = -0.59$, excluding highly enriched inclusions). Depleted inclusions with Ce/Y < 0.4 have generally high CO₂ contents, whereas enriched inclusions with Ce/Y > 0.55 have low CO₂ contents (Fig. 7c). This negative correlation implies that enriched melts have exsolved much more CO₂ than depleted melts prior to inclusion entrapment.

It is important to note, however, that binary mixing is unable to account for all of the variability in melt inclusion CO₂ contents. Although some primitive inclusions lie on a mixing line between a depleted, high-CO₂ end-member and an enriched, low-CO₂ end-member (Fig. 7c), many inclusions have significantly less CO₂ than predicted from binary mixing models (Fig. 7d). Therefore, while mixing and fractional crystallisation can account for melt inclusion trace element contents, additional CO₂ exsolution is required to explain the CO₂ contents of some melt inclusions.

CO₂/Nb values of ~400 in depleted melt inclusions are higher than values of $239 \pm 46$ reported for Siqueiros (Saal et al., 2002), but consistent with a value of $314 \pm 125$ reported for Borgarhraun, northern Iceland (Hauri et al., 2002) (Figs. 7a and 7b). High CO₂/Nb values suggest that depleted melts experienced little or possibly no CO₂ exsolution prior to inclusion entrapment, and provide the best current estimate of CO₂/Nb in primitive melts from the EVZ. In contrast, the low CO₂/Nb values in enriched melt inclusions (50–100) suggest that enriched melts experienced significant CO₂ exsolution prior to inclusion entrapment. The CO₂ content of ~300 ppm in enriched inclusions is consistent with a ~0.5 kbar depth of magma storage, according to the VOLATILECALC and SOLEX

H₂O–CO₂ solubility models of Newman and Lowenstern (2002) and Witham et al. (2012) respectively. However, the CO₂ content of ~1200 ppm in depleted inclusions suggests entrapment at ~1.5 kbar or greater.

Melt inclusion trace element systematics provide strong evidence for the juxtaposition and mixing of depleted and enriched melts within the same magma reservoir. It is not clear, however, when the exsolution of CO₂ from enriched melts occurred with respect to mixing with depleted melts. Two scenarios can be considered: firstly, that all CO₂ exsolution occurred while depleted and enriched melts were mixing; and secondly, that the majority of CO₂ exsolution from enriched melts occurred before mixing.

In the first scenario, geochemically variable and CO₂-rich melts would be delivered to a shallow magma reservoir at a depth recorded by the lowest CO₂ melt inclusions. Assuming that both depleted and enriched melts had a similar primary CO₂/Nb of ~400 and experienced no prior degassing, enriched melts would attain higher supersaturation pressures in a shallow reservoir. According to SOLEX, an undegassed depleted melt with 3.1 ppm Nb would reach a supersaturation pressure of ~1 kbar at a depth of 0.5 kbar, whereas an enriched melt with 4.2 ppm Nb would reach a supersaturation pressure of ~1.5 kbar. Therefore, enriched melts may have exsolved CO₂ more efficiently than depleted melts, generating a negative correlation between CO₂ and trace element enrichment. In this scenario, enriched melts would rapidly exsolve CO₂, resulting in the entrapment of low-CO₂ inclusions. In contrast, depleted melts would exsolve little or no CO₂ before entrapment, resulting in the entrapment of high-CO₂, supersaturated inclusions. Similar arguments have been put forward by Gonnermann and Mukhopadhyay (2007) to explain why the exsolution of CO₂ and noble gases from volatile-rich OIBs is more efficient than from volatile-poor MORBs. Recent experiments have indicated that supersaturation pressures of ~1.5 kbar are required for rapid CO₂ bubble nucleation to occur (Lensky et al., 2006; Pichavant et al., 2013), further suggesting that enriched melts are more likely than depleted melts to have reached the supersaturation required to trigger CO₂ exsolution.

In the second scenario, the diversity of melt inclusion compositions can be explained using a two-stage CO₂ exsolution model involving the injection of depleted and CO₂-supersaturated melts into a shallow reservoir containing enriched melts that have already exsolved much of their original CO₂ (Fig. 8). In this scenario, variability in both the trace element and CO₂ contents of primitive melt inclusions depends on the proportions in which end-members are mixed. Melt inclusions trapped before the second stage of CO₂ exsolution have CO₂ contents that lie along mixing lines (Figs. 7c and 7d). Inclusions trapped during the second stage of syn-mixing CO₂ exsolution have CO₂ concentrations that lie off of mixing lines towards lower CO₂ contents (Figs. 7c and 7d).

Although most primitive melt inclusion compositions can be explained with a single mixing event, highly-enriched and evolved melt inclusion compositions cannot (Fig. 7c). Injection of highly-enriched melts at a later stage could explain the presence of highly-enriched inclusions, which may not be related simply to the rest of the primitive inclusion population. The disparity between the mean primitive melt inclusion composition (Ce/Y ~ 0.47) and the matrix glass composition (Ce/Y ~ 0.65) suggests that the primitive Skuggafjöll magma interacted with more enriched melts prior to eruption. It is also possible that further batches of CO₂-supersaturated melt were injected when the magma was more evolved, explaining the CO₂-rich evolved melt inclusion that lies on a mixing line between depleted and highly-enriched melts (Fig. 7c).

While it is difficult to rule out either of these scenarios for generating a negative correlation between trace element enrichment and CO₂ content, they share two important features: firstly, mix-
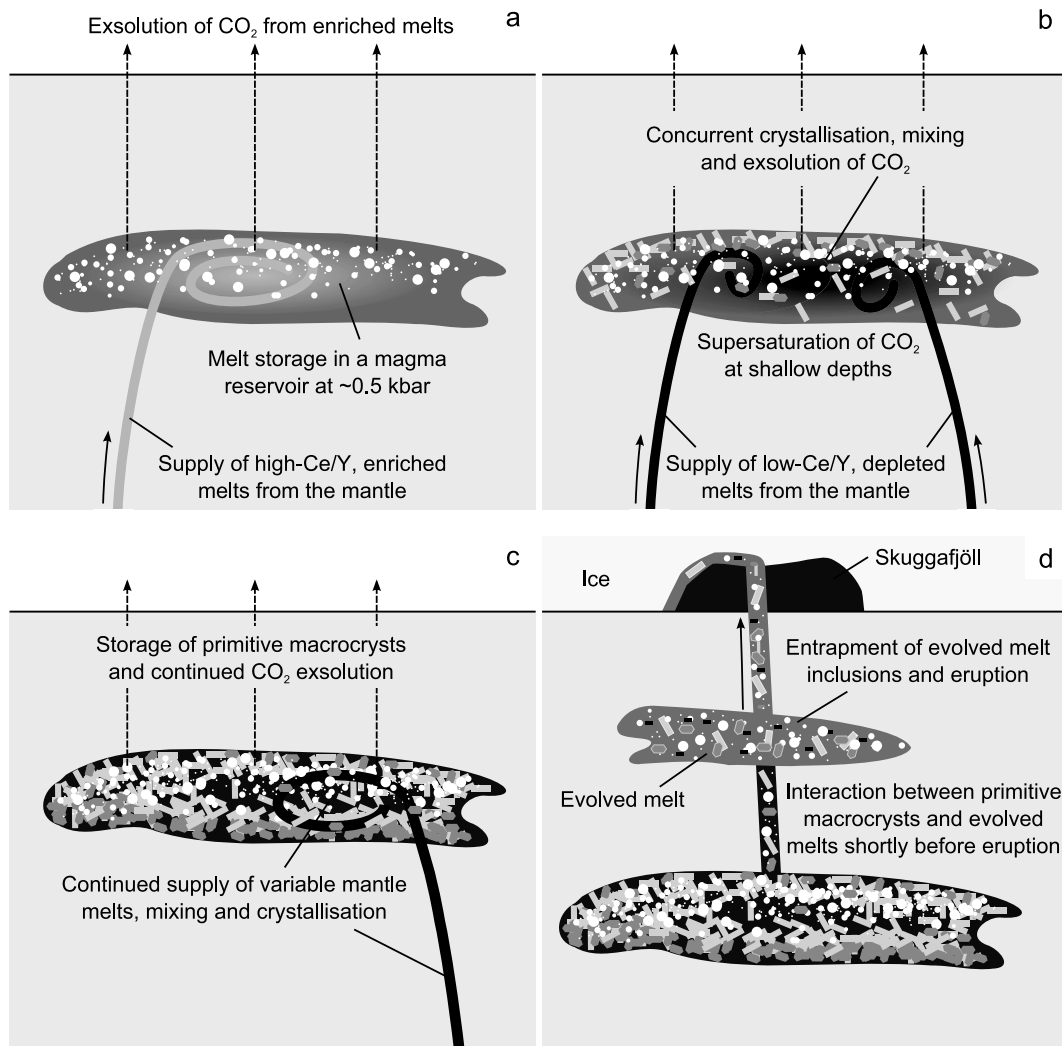
**Fig. 8.** Summary cartoon outlining the magmatic processes inferred for a scenario where enriched melts exsolved most of their initial $CO_2$ before mixing. (a) Storage of an enriched melt at shallow levels ($\sim$0.5 kbar) in the crust. The enriched melt loses much of its initial $CO_2$ content. Enriched melt therefore attain an equilibrium $CO_2$ content of $\sim$300 ppm and have a low $CO_2$/Nb values of 50–100. (b) Injection of a depleted and $CO_2$-supersaturated melt with $CO_2$/Nb $\sim$ 400. Melt inclusions are trapped as the melts stir, mix, cool and crystallise. $CO_2$-supersaturated melts exsolve $CO_2$ during mixing, leading to the trapping of melt inclusions with a range of $CO_2$-supersaturated to $CO_2$-saturated compositions. (c) Storage of primitive macrocrysts while injection of variable mantle melts into the magma reservoir continues. (d) Interaction of macrocrysts containing primitive inclusions with more evolved and enriched melts shortly before eruption and trapping of evolved melt inclusions.

ing controls melt $CO_2$ contents, whether by determining the extent of supersaturation or by stirring together melts that have experienced varying amounts of prior $CO_2$ exsolution; and secondly, depleted inclusions trap $CO_2$-supersaturated melts. In order to consider whether the trapping of $CO_2$-supersaturated melt inclusions is feasible, it is important to consider how $CO_2$ supersaturation may develop and be maintained in ascending and mixing basalts.

### 4.5. $CO_2$ supersaturation in basaltic melts during ascent and mixing

It is well established that $CO_2$ concentrations in submarine basaltic glasses often exceed equilibrium concentrations predicted from solubility models (Fine and Stolper, 1986; Dixon et al., 1988; Cartigny et al., 2008; Helo et al., 2011; Wanless and Shaw, 2012; Soule et al., 2012, 2013). It is therefore possible for basalts to be transported from magma reservoirs to the surface faster than $CO_2$ can exsolve and to become $CO_2$-supersaturated. In recent experiments, Pichavant et al. (2013) investigated vesiculation of basalts from Stromboli by simulating ascent from 2–2.5 kbar to 0.25–0.5 kbar. Although the compositions investigated were more hydrous than those at Skuggafjöll (2.7–3.8 wt% $H_2O$ versus $\sim$0.4 wt%), the following observations are particularly rele-

vant: firstly, $CO_2$ concentrations of up to one order of magnitude higher than solubility were generated at decompression rates of 0.25–1.5 m/s; secondly, these $CO_2$ excesses correspond to supersaturation pressures of $\sim$1.5 kbar; and thirdly, $CO_2$ exsolution was primarily controlled by vesicularity. At low vesicularities, $CO_2$ exsolution was limited by the rate of $CO_2$ diffusion through the melt rather than the rate of $CO_2$ transfer across melt/vesicle interfaces, resulting in disequilibrium degassing (e.g. Mangan and Sisson, 2000). Low vesicularities were generated in experimental runs with high $CO_2$ and low $H_2O$ contents, where $H_2O$ exsolution was inhibited and vesicle nucleation therefore reduced: $H_2O$ vesicle nucleation is more favourable than $CO_2$ vesicle nucleation (Bottinga and Javoy, 1990; Bai et al., 2008).

Depleted melts from Skuggafjöll have similar $CO_2$ contents to the experimental melts of Pichavant et al. (2013), but much lower $H_2O$ contents. It follows that vesicularity would be very low in melts supplying the Skuggafjöll magma reservoir and that $CO_2$ exsolution would, as a consequence, be diffusion-limited and inefficient. Therefore, not only would it be possible for $CO_2$ supersaturation to develop during supply of basalts to shallow magma reservoirs, but it should perhaps be expected in $H_2O$-poor and $CO_2$-rich systems.

In order to assess how long a depleted and $CO_2$-supersaturated melt might maintain $CO_2$ supersaturation following intrusion into a magma reservoir at $\sim$0.5 kbar, calculations were performed using the relationship provided by Epstein and Plesset (1950) for the stability of bubbles in undersaturated or supersaturated solutions:

$$(r/r_0)^2 = 1 + \left[2D(c_i - c_s)/\rho r_0 2\right]t \qquad (3)$$

where $r_0$ is the initial vesicle radius, $D$ is the diffusion coefficient of $CO_2$, $(c_i - c_s)$ is the difference between the initial $CO_2$-supersaturated content ($c_i$; 1250 ppm) and the $CO_2$-saturated content at equilibrium ($c_s$; 300 ppm), $\rho$ is the density of the $CO_2$ in vesicles and $r$ is the vesicle radius after time $t$. $r_0$ is assumed to be small (1 nm) because vesicles are not inherited from previous degassing events. Increasing the initial radius by up to a few orders of magnitude does not significantly affect results, as vesicle-melt equilibrium is rapidly achieved. $D$ was calculated as $7.54 \times 10^{-12}$ m/s$^2$ using Eq. (11) of Ni and Keppler (2013) at 0.5 kbar and 1200 °C. $\rho$ was calculated using Holland and Powell (1991) at 0.5 kbar and 1200 °C. In order to account for the decrease in $(c_i - c_s)$ with time as $CO_2$ exsolves, we employed the technique used by Soule et al. (2012, 2013) where $(c_i - c_s)$ was recalculated after each time step. However, there are two main sources of uncertainty in using the relationship of Epstein and Plesset (1950) to estimate timescales of $CO_2$ exsolution.

Firstly, in order to determine how much $CO_2$ is lost from a given volume of melt, an estimate of the number density of vesicles ($N_t$) is required. Although $N_t$ values for stored melts are poorly constrained, it is possible to estimate maximum $N_t$ values from vesicle size distributions (VSDs) calculated from erupted lavas. Given that nucleation rates are likely to be higher during eruption than during deep storage, lavas quenched shortly after eruption record the highest values of $N_t$ experienced by the magma, and thus provide an upper limit on $N_t$ at depth. The size of vesicles in a magma can be described by the following relationship (Sarda and Graham, 1990; Mangan et al., 1993):

$$n = n^0 \exp(-L/Gt) \qquad (4)$$

where $n$ is the number density of bubbles of a given size per unit volume of melt, $L$ is the bubble diameter, $n^0$ is the number density of nuclei, $G$ is the mean growth rate of bubbles, and $t$ is time. $N_t$ can then be estimated using the expression:

$$N_t = n^0 Gt \qquad (5)$$

where $n^0$ is given by the intercept of a VSD when plotted as $L$ versus $\ln(n)$, and $-1/Gt$ is the slope (Mangan et al., 1993). VSDs calculated for two thin sections from Skuggafjöll are shown in Fig. 9a. VSD calculation methods are provided in the supplementary material. $N_t$ values of $4.5 \times 10^3$ cm$^{-3}$ and $2.2 \times 10^4$ cm$^{-3}$ calculated from VSDs are similar to average values of $7.9 \times 10^3$ cm$^{-3}$ and $4.0 \times 10^3$ cm$^{-3}$ for MORB and Kīlauea respectively calculated using similar techniques (Sarda and Graham, 1990; Mangan et al., 1993). Values of $N_t$ relevant to $CO_2$ exsolution at depth within the Skuggafjöll are likely to have been significantly smaller than these maximum estimates.

Secondly, calculations using the relationship of Epstein and Plesset (1950) assume that all vesicles have nucleated before the onset of $CO_2$ exsolution, and that no further nucleation occurs whilst vesicles are growing. Both of these assumptions are likely to be incorrect. Vesicle nucleation will only start once melts reach a critical supersaturation pressure during ascent and will continue as long as melts are sufficiently supersaturated regardless of whether vesicle growth is also occurring. The $CO_2$ exsolution timescales calculated here are thus minimum estimates for the following reasons: firstly, $N_t$ values estimated from erupted basalts represent maximum vesicle number densities; and secondly, assuming that
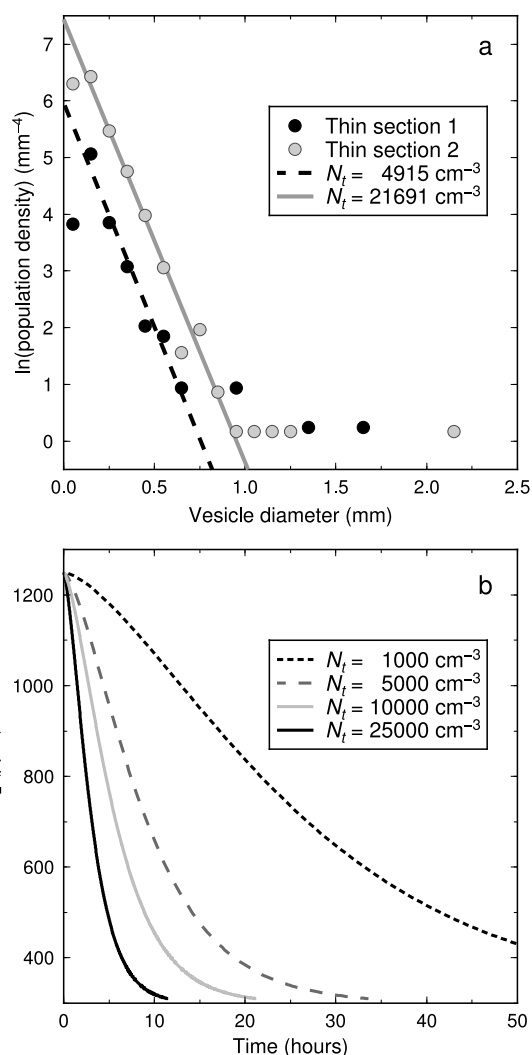


**Fig. 9.** (a) Vesicle size distributions (VSDs) for two thin sections from Skuggafjöll. Data are shown as circles. Linear regressions through VSDs used to calculated $N_t$ values are shown as lines. Data from undersampled bins containing the smallest and largest vesicles were not included in regressions. The two thin sections record $N_t$ values of $4.5 \times 10^3$ cm$^{-3}$ and $2.2 \times 10^4$ cm$^{-3}$. (b) Plot showing how the $CO_2$ content of $CO_2$-supersaturated basalts with an initial $CO_2$ content of 1250 ppm evolve as they exsolve $CO_2$ in a shallow magma reservoir at 0.5 kbar. $CO_2$ exsolution trajectories were calculated range of vesicle number densities ($N_t$). A maximum $N_t$ value of $2.5 \times 10^4$ cm$^{-3}$ was estimated from the VSDs shown in (a). $N_t$ values for deep $CO_2$ exsolution are likely to be much lower, resulting in longer exsolution timescales.

nucleation was complete at the time of intrusion will lead to $N_t$ being overestimated.

Estimated timescales for $CO_2$ exsolution are presented in Fig. 9b. Even under the conditions most conducive to $CO_2$ loss, (i.e. high $N_t$), significant quantities of $CO_2$ ($>$1000 ppm) may be retained by intruding melts for hours after intrusion. If vesicle nucleation rates were low and vesicle number densities were significantly lower than the maximum estimate of $2.2 \times 10^4$ cm$^{-3}$, $CO_2$ supersaturation could be maintained for days after intrusion to shallow levels ($\sim$0.5 kbar in this case). Coupling of $CO_2$ exsolution and mixing processes suggests that crystallisation and melt inclusion entrapment occurred on the same time scale.

### 4.6. Implications for the interpretation of volatile data in melt inclusions

Although melt inclusions provide important glimpses into the behaviour of volatiles during the deep evolution of magmas, errors

may arise during interpretation if volatile species are considered in isolation from trace elements. For example, the large variation of $CO_2$ contents at a constant $H_2O$ content shown in Fig. 5a could be interpreted as evidence for open system degassing (e.g. Dixon and Stolper, 1995), entrapment at a range of pressures in a complex magma reservoir, or possibly as gas flushing by $CO_2$-rich gases sourced deeper in the plumbing system (e.g. Métrich and Wallace, 2008). However, the correlation of $CO_2$ with measures of primary melt variability that can only be fractionated significantly during mantle melting, such as Ce/Y, provides the crucial evidence that melt mixing plays an important role in controlling the $CO_2$ content of melt inclusions from Skuggafjöll.

## 5. Conclusions

The effect of magma mixing on the $CO_2$ contents of primitive basalts has been investigated by measuring both volatiles and trace elements in a suite of olivine-hosted melt inclusions from the Skuggafjöll eruption in the EVZ of Iceland. The majority of melt inclusions are more primitive than the erupted carrier liquid. Trace element variability in the melt inclusion population can be accounted for by a combination of mixing between depleted and enriched end-members and fractional crystallisation. Melt inclusion trace element enrichment correlates negatively with $CO_2$ content: depleted melt inclusions have high and possibly original $CO_2$ contents and $CO_2/Nb$ values, whereas enriched melt inclusions have low $CO_2$ contents and $CO_2/Nb$ values. The total $CO_2$ content of melt inclusions is not affected by $CO_2$ sequestration into inclusion-hosted bubbles because of rapid quenching shortly after eruption. The negative correlation between trace element enrichment and $CO_2$ content may be generated by efficient exsolution of $CO_2$ from enriched melts either during or before mixing with $CO_2$-supersaturated depleted melts. That trace element-$CO_2$ systematics cannot be explained by binary mixing alone suggests that at least some $CO_2$ exsolution occurred concurrently with mixing and crystallisation. During ascent within the crust, $H_2O$-poor basalts are likely to become $CO_2$-supersaturated, and may remain $CO_2$-supersaturated for hours to days after transport to shallow magma reservoirs because of inefficient $CO_2$ exsolution. Magma mixing processes are thus able produce $H_2O$–$CO_2$ systematics similar to those arising from degassing processes alone. Preservation of $CO_2$ supersaturation in ascending and mixing melts may lead to overestimation of entrapment depths derived from the volatile contents of melt inclusions. Nevertheless, the identification of $CO_2$ supersaturation in melt inclusions has the potential to place constraints on timescales of crystallisation and inclusion entrapment.

## Acknowledgements

## Appendix A. Supplementary material

Supplementary material related to this article can be found online at http://dx.doi.org/10.1016/j.epsl.2014.05.050.

## References

Albarède, F., 1996. High resolution geochemical stratigraphy of Mauna Kea flows from the Hawaii Scientific Drilling Project core. J. Geophys. Res., Solid Earth 101 (B5), 11841–11853.

Anderson, A.L., Brown, G.G., 1993. $CO_2$ contents and formation pressures of some Kilauean melt inclusions. Am. Mineral. 78 (1), 794–803.

Bai, L., Baker, D., Rivers, M., 2008. Experimental study of bubble growth in Stromboli basalt melts at 1 atm. Earth Planet. Sci. Lett. 267 (3–4), 533–547.

Bédard, J.H., 2005. Partitioning coefficients between olivine and silicate melts. Lithos 83 (3–4), 394–419.

Bindeman, I.N., Davis, A.M., 2000. Trace element partitioning between plagioclase and melt: investigation of dopant influence on partition behavior. Geochim. Cosmochim. Acta 64 (16), 2863–2878.

Blake, S., 1984. Volatile oversaturation during the evolution of silicic magma chambers as an eruption trigger. J. Geophys. Res. 89, 8237–8244.

Blundy, J.D., Wood, B.J., 1991. Crystal-chemical controls on the partitioning of Sr and Ba between plagioclase feldspar, silicate melts, and hydrothermal solutions. Geochim. Cosmochim. Acta 55 (1), 193–209.

Bottinga, Y., Javoy, M., 1990. Mid-ocean ridge basalt degassing: bubble nucleation. J. Geophys. Res., Solid Earth 95, 5125–5131.

Bucholz, C.E., Gaetani, G.A., Behn, M.D., Shimizu, N., 2013. Post-entrapment modification of volatiles and oxygen fugacity in olivine-hosted melt inclusions. Earth Planet. Sci. Lett. 374, 145–155.

Cartigny, P., Pineau, F., Aubaud, C., Javoy, M., 2008. Towards a consistent mantle carbon flux estimate: insights from volatile systematics ($H_2O/Ce$, $\delta D$, $CO_2/Nb$) in the North Atlantic mantle (14°N and 34°N). Earth Planet. Sci. Lett. 265 (3–4), 672–685.

Costa, F., Morgan, D., 2010. Time constraints from chemical equilibration in magmatic crystals. In: Timescales of Magmatic Processes. Wiley-Blackwell, pp. 125–159. Chapter 7.

Danyushevsky, L.V., 2001. The effect of small amounts of $H_2O$ on crystallisation of mid-ocean ridge and backarc basin magmas. J. Volcanol. Geotherm. Res. 110 (3–4), 265–280.

Danyushevsky, L.V., Della-Pasqua, F.N., Sokolov, S., 2000. Re-equilibration of melt inclusions trapped by magnesian olivine phenocrysts from subduction-related magmas: petrological implications. Contrib. Mineral. Petrol. 138 (1), 68–83.

Danyushevsky, L.V., McNeill, A.W., Sobolev, A.V., 2002. Experimental and petrological studies of melt inclusions in phenocrysts from mantle-derived magmas: an overview of techniques, advantages and complications. Chem. Geol. 183 (1–4), 5–24.

Danyushevsky, L.V., Plechov, P., 2011. Petrolog3: integrated software for modeling crystallization processes. Geochem. Geophys. Geosyst. 12 (7).

Dixon, J.E., 1997. Degassing of alkalic basalts. Am. Mineral. 82, 368–378.

Dixon, J.E., Clague, D.A., 2001. Volatiles in basaltic glasses from Loihi Seamount, Hawaii: evidence for a relatively dry plume component. J. Petrol. 42 (3), 627–654.

Dixon, J.E., Clague, D.A., Cousens, B., Monsalve, M.L., Uhl, J., 2008. Carbonatite and silicate melt metasomatism of the mantle surrounding the Hawaiian plume: evidence from volatiles, trace elements, and radiogenic isotopes in rejuvenated-stage lavas from Niihau, Hawaii. Geochem. Geophys. Geosyst. 9 (9), 1–34.

Dixon, J.E., Stolper, E.M., 1995. An experimental study of water and carbon dioxide solubilities in mid-ocean ridge basaltic liquids. Part II: Applications to degassing. J. Petrol. 36 (6), 1633–1646.

Dixon, J.E., Stolper, E.M., Delaney, J.R., 1988. Infrared spectroscopic measurements of $CO_2$ and $H_2O$ in Juan de Fuca Ridge basaltic glasses. Earth Planet. Sci. Lett. 90, 87–104.

Eggler, D.H., 1976. Does $CO_2$ cause partial melting in the low-velocity layer of the mantle? Geology 4, 69–72.

Epstein, P.S., Plesset, M.S., 1950. On the stability of gas bubbles in liquid–gas solutions. J. Chem. Phys. 18 (11), 1505.

Fine, G., Stolper, E., 1986. Dissolved carbon dioxide in basaltic glasses: concentrations and speciation. Earth Planet. Sci. Lett. 76, 263–278.

Frezzotti, M.L., Tecce, F., Casagli, A., 2012. Raman spectroscopy for fluid inclusion analysis. J. Geochem. Explor. 112, 1–20.

Gaetani, G.A., O'Leary, J.A., Shimizu, N., Bucholz, C.E., Newville, M., 2012. Rapid reequilibration of $H_2O$ and oxygen fugacity in olivine-hosted melt inclusions. Geology 40 (10), 915–918.

Giordano, D., Russell, J., Dingwell, D., 2008. Viscosity of magmatic liquids: a model. Earth Planet. Sci. Lett. 271 (1–4), 123–134.

Gonnermann, H.M., Mukhopadhyay, S., 2007. Non-equilibrium degassing and a primordial source for helium in ocean-island volcanism. Nature 449 (7165), 1037–1040.

Green, D.H., 1973. Experimental melting studies on a model upper mantle composition at high pressure under water-saturated and water-undersaturated conditions. Earth Planet. Sci. Lett. 19, 37–53.

Gurenko, A.A., Chaussidon, M., 1995. Enriched and depleted primitive melts included in olivine from Icelandic tholeiites – Origin by melting of a single manlte column. Geochim. Cosmochim. Acta 59 (14), 2905–2917.

Gurenko, A.A., Sobolev, A.V., 2006. Crust-primitive magma interaction beneath neo-volcanic rift zone of Iceland recorded in gabbro xenoliths from Midfell, SW Iceland. Contrib. Mineral. Petrol. 151 (5), 495–520.

Hansen, H., Grönvold, K., 2000. Plagioclase ultraphyric basalts in Iceland: the mush of the rift. J. Volcanol. Geotherm. Res. 98 (1–4), 1–32.

Hansteen, T.H., Klugel, A., 2008. Fluid inclusion thermobarometry as a tracer for magmatic processes. Rev. Mineral. Geochem. 69 (1), 143–177.

Hartley, M.E., Maclennan, J., Edmonds, M.E., Thordarson, T., 2014. Reconstructing the deep $CO_2$ degassing behaviour of large basaltic fissure eruptions. Earth Planet. Sci. Lett. 393, 120–131.

Hauri, E.H., 2002. SIMS analysis of volatiles in silicate glasses: 2. Isotopes and abundances in Hawaiian melt inclusions. Chem. Geol. 183 (1–4), 115–141.

Hauri, E.H., Grönvold, K., Öskarsson, N., McKenzie, D., 2002. Abundance of carbon in the Icelandic mantle: constraints from melt inclusions. In: American Geophysical Union, Spring Meeting, pp. V51D–03.

Helo, C., Longpré, M.-A., Shimizu, N., Clague, D.A., Stix, J., 2011. Explosive eruptions at mid-ocean ridges driven by $CO_2$-rich magmas. Nat. Geosci. 4 (4), 260–263.

Hill, E., Blundy, J.D., Wood, B.J., 2010. Clinopyroxene-melt trace element partitioning and the development of a predictive model for HFSE and Sc. Contrib. Mineral. Petrol. 161 (3), 423–438.

Holland, T., Powell, R., 1991. A Compensated-Redlich-Kwong (CORK) equation for volumes and fugacities of $CO_2$ and $H_2O$ in the range 1 bar to 50 kbar and 100–1600 °C. Contrib. Mineral. Petrol. 109, 265–273.

Höskuldsson, A., Sparks, R.S.J., Carroll, M.R., 2006. Constraints on the dynamics of subglacial basalt eruptions, from geological and geochemical observations at Kverkfjöll, NE-Iceland. Bull. Volcanol. 68, 689–701.

Hubbard, A., Sugden, D., Dugmore, A., Norddahl, H., Pétursson, H.G., 2006. A modelling insight into the Icelandic Last Glacial Maximum ice sheet. Quat. Sci. Rev. 25 (17–18), 2283–2296.

Jakobsson, S.P., 1979. Petrology of recent basalts of the Eastern Volcanic Zone, Iceland. Acta Nat. Isl. 26, 1–103.

Jakobsson, S.P., Gudmundsson, M.T., 2008. Subglacial and intraglacial volcanic formations in Iceland. Jökull 58, 179–196.

Koleszar, A.M., Saal, A.E., Hauri, E.H., Nagle, A.N., Liang, Y., Kurz, M.D., 2009. The volatile contents of the Galapagos plume; evidence for $H_2O$ and F open system behavior in melt inclusions. Earth Planet. Sci. Lett. 287 (3–4), 442–452.

Lensky, N., Niebo, R., Holloway, J., Lyakhovsky, V., Navon, O., 2006. Bubble nucleation as a trigger for xenolith entrapment in mantle melts. Earth Planet. Sci. Lett. 245 (1–2), 278–288.

Lowenstern, J.B., 1995. Applications of silicate-melt inclusions to the study of magmatic volatiles. In: Thompson, J.F.H. (Ed.), Magmas, Fluids, and Ore Deposits. In: Mineral Association Canada Short Course Series, vol. 23, pp. 71–99. Chapter 4.

Maclennan, J., 2008a. Concurrent mixing and cooling of melts under Iceland. J. Petrol. 49 (11), 1931–1953.

Maclennan, J., 2008b. Lead isotope variability in olivine-hosted melt inclusions from Iceland. Geochim. Cosmochim. Acta 72 (16), 4159–4176.

Maclennan, J., McKenzie, D., Hilton, F., Grönvold, K., Shimizu, N., 2003. Geochemical variability in a single flow from northern Iceland. J. Geophys. Res. 108 (B1), 1–21.

Mangan, M.T., Cashman, K.V., Newman, S., 1993. Vesiculation of basaltic magma during eruption. Geology 21, 157–160.

Mangan, M.T., Sisson, T., 2000. Delayed, disequilibrium degassing in rhyolite magma: decompression experiments and implications for explosive volcanism. Earth Planet. Sci. Lett. 183 (3–4), 441–455.

McKenzie, D., O'Nions, R.K., 1998. Melt production beneath oceanic islands. Phys. Earth Planet. Inter. 107 (1–3), 143–182.

Métrich, N., Wallace, P.J., 2008. Volatile abundances in basaltic magmas and their degassing paths tracked by melt inclusions. Rev. Mineral. Geochem. 69 (1), 363–402.

Moune, S., Sigmarsson, O., Schiano, P., Thordarson, T., Keiding, J.K., 2012. Melt inclusion constraints on the magma source of Eyjafjallajökull 2010 flank eruption. J. Geophys. Res. 117, 1–13.

Neave, D.A., Passmore, E., Maclennan, J., Fitton, G., Thordarson, T., 2013. Crystal-melt relationships and the record of deep mixing and crystallization in the AD 1783 Laki Eruption, Iceland. J. Petrol. 54, 1661–1690.

Newman, S., Lowenstern, J.B., 2002. VolatileCalc: a silicate melt-$H_2O$–$CO_2$ solution model written in Visual Basic for excel. Comput. Geosci. 28, 597–604.

Ni, H., Keppler, H., 2013. Carbon in silicate melts. Rev. Mineral. Geochem. 75, 251–287.

Ochs, F.A., Lange, R.A., 1997. The partial molar volume, thermal expansivity, and compressibility of $H_2O$ in $NaAlSi_3O_8$ liquid: new measurements and an internally consistent model. Contrib. Mineral. Petrol. 129, 155–165.

Owen, J., Tuffen, H., McGarvie, D.W., 2012. Using dissolved $H_2O$ in rhyolitic glasses to estimate palaeo-ice thickness during a subglacial eruption at Bláhnúkur (Torfajökull, Iceland). Bull. Volcanol. 74, 1355–1378.

Passmore, E., 2009. Feeding large eruptions: crystallisation, mixing and degassing in Icelandic magma chambers. Ph.D. thesis. University of Edinburgh.

Pichavant, M., Carlo, I., Rotolo, S.G., Scaillet, B., Burgisser, A., Gall, N., Martel, C., 2013. Generation of $CO_2$-rich melts during basalt magma ascent and degassing. Contrib. Mineral. Petrol. 166 (2), 545–561.

Portnyagin, M., Almeev, R., Matveev, S., Holtz, F., 2008. Experimental evidence for rapid water exchange between melt inclusions in olivine and host magma. Earth Planet. Sci. Lett. 272 (3–4), 541–552.

Putirka, K.D., 2005. Igneous thermometers and barometers based on plagioclase + liquid equilibria: tests of some existing models and new calibrations. Am. Mineral. 90 (1991), 336–346.

Qin, Z., Lu, F., Anderson Jr., T., 1992. Diffusive reequilibration of melt and fluid inclusions. Am. Mineral. 77, 565–576.

Roedder, E., 1979. Origin and significance of magmatic inclusions. Bull. Minér. 102, 487–510.

Roedder, P.L., 1984. Fluid inclusions. Mineral. Soc. Am. Monograph 12, 644.

Roggensack, K., Hervig, R.L., McKnight, S.B., Williams, S.N., 1997. Explosive basaltic volcanism from Cerro Negro Volcano: influence of volatiles on eruptive style. Science 277, 1639–1642.

Rosso, K.M., Bodnar, R.J., 1995. Microthermometric and Raman spectroscopic detection limits of $CO_2$ in fluid inclusions and the Raman spectroscopic characterization of $CO_2$. Geochim. Cosmochim. Acta 59 (19), 3961–3975.

Rudge, J.F., Maclennan, J., Stracke, A., 2013. The geochemical consequences of mixing melts from a heterogeneous mantle. Geochim. Cosmochim. Acta 114, 112–143.

Saal, A.E., Hauri, E.H., Langmuir, C.H., Perfit, M.R., 2002. Vapour undersaturation in primitive mid-ocean-ridge basalt and the volatile content of Earth's upper mantle. Nature 419, 451–455.

Sarda, P., Graham, D., 1990. Mid-ocean ridge popping rocks: implications for degassing at ridge crests. Earth Planet. Sci. Lett. 97 (3–4), 268–289.

Shaw, A.M., Behn, M.D., Humphris, S.E., Sohn, R.A., Gregg, P.M., 2010. Deep pooling of low degree melts and volatile fluxes at the 85°E segment of the Gakkel Ridge: evidence from olivine-hosted melt inclusions and glasses. Earth Planet. Sci. Lett. 289 (3–4), 311–322.

Shaw, A.M., Hauri, E.H., Fischer, T.P., Hilton, D.R., Kelley, K.A., 2008. Hydrogen isotopes in Mariana arc melt inclusions: implications for subduction dehydration and the deep-Earth water cycle. Earth Planet. Sci. Lett. 275 (1–2), 138–145.

Shishkina, T.A., Botcharnikov, R.E., Holtz, F., Almeev, R.R., Portnyagin, M.V., 2010. Solubility of $H_2O$- and $CO_2$-bearing fluids in tholeiitic basalts at pressures up to 500 MPa. Chem. Geol. 277 (1–2), 115–125.

Slater, L., McKenzie, D., Grönvold, K., Shimizu, N., 2001. Melt generation and movement beneath Theistareykir, NE Iceland. J. Petrol. 42 (2), 321–354.

Soule, S.A., Fornari, D.J., Perfit, M.R., Kurz, M.D., 2013. Reply to comment on "$CO_2$ variability in mid-ocean ridge basalts from syn-emplacement degassing: constraints on eruption dynamics" by Soule et al. [Earth Planet. Sci. Lett. (2012) 327–328, 39–49]. Earth Planet. Sci. Lett. 400, 1–2.

Soule, S.A., Nakata, D.S., Fornari, D.J., Fundis, A.T., Perfit, M.R., Kurz, M.D., 2012. $CO_2$ variability in mid-ocean ridge basalts from syn-emplacement degassing: constraints on eruption dynamics. Earth Planet. Sci. Lett. 327–328, 39–49.

Steele-Macinnis, M., Esposito, R., Bodnar, R., 2011. Thermodynamic model for the effect of post-entrapment crystallization on the $H_2O$–$CO_2$ systematics of vapor-saturated, silicate melt inclusions. J. Petrol. 52 (12), 2461–2482.

Thomson, A., Maclennan, J., 2013. The distribution of olivine compositions in Icelandic basalts and picrites. J. Petrol. 54 (4), 745–768.

Thordarson, T., Larsen, G., 2007. Volcanism in Iceland in historical time: volcano types, eruption styles and eruptive history. J. Geodyn. 43 (1), 118–152.

Tuffen, H., Owen, J., Denton, J., 2010. Magma degassing during subglacial eruptions and its use to reconstruct palaeo-ice thicknesses. Earth-Sci. Rev. 99 (1–2), 1–18.

Wanless, V.D., Shaw, A.M., 2012. Lower crustal crystallization and melt evolution at mid-ocean ridges. Nat. Geosci. 5 (9), 1–5.

Waters, C.L., Sims, K.W.W., Perfit, M.R., Blichert-Toft, J., Blusztajn, J., 2011. Perspective on the genesis of E-MORB from chemical and isotopic heterogeneity at 9–10°N East Pacific Rise. J. Petrol. 52 (3), 565–602.

Winpenny, B., Maclennan, J., 2011. A Partial record of mixing of mantle melts preserved in Icelandic phenocrysts. J. Petrol. 52 (9), 1791–1812.

Witham, F., Blundy, J.D., Kohn, S.C., Lesne, P., Dixon, J.E., Churakov, S.V., Botcharnikov, R., 2012. SolEx: a model for mixed COHSCl-volatile solubilities and exsolved gas compositions in basalt. Comput. Geosci. 45, 87–97.

Wood, B.J., Blundy, J.D., 1997. A predictive model for rare earth element partitioning between clinopyroxene and anhydrous silicate melt. Contrib. Mineral. Petrol. 129 (2–3), 166–181.

Woods, A., 1995. The dynamics of explosive volcanic eruptions. Rev. Geophys. 33 (4), 495–530.

Workman, R., Hart, S., 2005. Major and trace element composition of the depleted MORB mantle (DMM). Earth Planet. Sci. Lett. 231 (1–2), 53–72.

Workman, R.K., Hauri, E.H., Hart, S.R., Wang, J., Blusztajn, J., 2006. Volatile and trace elements in basaltic glasses from Samoa: implications for water distribution in the mantle. Earth Planet. Sci. Lett. 241 (3–4), 932–951.

Wyllie, P.J., Huang, W.L., 1976. Carbonation and melting reactions in the system $CaO$–$MgO$–$SiO_2$–$CO_2$ at mantle pressures with geophysical and petrological applications. Contrib. Mineral. Petrol. 107, 79–107.

Zindler, A., Staudigel, H., Batiza, R., 1984. Isotope and trace element geochemistry of young Pacific seamounts: implications for the scale of upper mantle heterogeneity. Earth Planet. Sci. Lett. 70 (2), 175–195.